Final Draft
of the original manuscript:

Tie, D.; Guan, R.; Liu, H.; Cipriano, A.; Liu, Y.; Wang, Q.; Huang, Y.; Hort, N.:
An in vivo study on the metabolism and osteogenic activity of bioabsorbable Mg–1Sr alloy
In: Acta Biomaterialia (2015) Elsevier

DOI: 10.1016/j.actbio.2015.11.014

An in vivo study on the metabolism and osteogenic activity of bioabsorbable Mg–1Sr alloy

D. Tie[1] and R. Guan[1], H. Liu[2], A. Cipriano[2], Y. Liu[3], Q. Wang[1], Y. Huang[4], N. Hort[4]

[1]School of Materials and Metallurgy, Northeastern University, Shenyang, China
[2]Department of Bioengineering, University of California, Riverside, USA
[3]Surgery Center, Hospital of China Medical University, Shenyang, China
[4]Magnesium Innovation Center, Helmholtz-Zentrum Geesthacht, Geesthacht, Germany

Abstract

Previous studies indicated that local delivery of strontium effectively increased bone quality and formation around osseointegrating implants. Therefore, implant materials with long-lasting and controllable strontium release are avidly pursued. The central objective of the present study was to investigate the in vivo biocompatibility, metabolism and osteogenic activity of the bioabsorbable Mg–1Sr (wt.%, nominal composition) alloy for bone regeneration. The general corrosion rate of the alloy implant as a femoral fracture fixation device was 0.55 $\pm$ 0.03 mm y^{-1} (mean value $\pm$ standard deviation) in New Zealand White rabbits which meet the bone implantation requirements and can be adjusted by material processing methods. All rabbits survived and the histological evaluation showed no abnormal physiology or diseases 16 weeks post-implantation. The degradation process of the alloy did not significantly alter 16 primary indexes of hematology, cardiac damage, inflammation, hepatic functions and metabolic process. Significant increases in peri-implant bone volume and direct bone-to-implant contact (48.3% $\pm$ 15.3% and 15.9% $\pm$ 5.6%, respectively) as well as the expressions of four osteogenesis related genes (runt-related transcription factor 2, alkaline phosphatase, osteocalcin, and collagen, type I, alpha 1) were observed after 16 weeks implantation for the Mg–1Sr group when compared to the pure Mg group. The sound osteogenic properties of the Mg–1Sr alloy by long-lasting and controllable Sr release suggesting a very attractive clinical potential.

Statement of significance

Sr (strontium) has exhibited pronounced effects to reduce the bone fracture risk in osteoporotic patients. Nonetheless, long-lasting local Sr release is hardly achieved by traditional methods like surface treatment. Therefore, a more efficient Sr local delivery platform is in high clinical demand. The stable and adjustable degradation process of Mg alloy makes it an ideal Sr delivery platform. We combine the well-known osteogenic properties of strontium with magnesium to manufacture bioabsorbable Mg–1Sr alloy with stable Sr release based on our previous studies. The in vitro and in vivo results both showed the alloy's suitable degradation rate and biocompatibility, and the sound osteogenic properties and stimulation effect on bone formation suggest its very attractive clinical potential.

1 Introduction

Strontium (Sr) has aroused tremendous clinical interests especially after the development of the anti-osteoporosis drug strontium ranelate which exhibits pronounced effects to reduce the bone fracture risk in osteoporotic patients [1,2]. Sr increases osteoblast replication, differentiation, and bone matrix mineralization relying on calcium sensing receptor dependent mechanism [3–5]. Previous studies incorporated Sr into calcium phosphate coatings or bioactive glasses to stimulate the bone formation [6–9]. Nonetheless, long-lasting Sr release at a reasonably constant rate is hardly achieved in these cases due to low and unstable solubility of Sr in calcium phosphates and glasses [10,11]. In this respect, a more efficient delivery platform with controlled Sr release is in high clinical demand.

On the other hand, magnesium (Mg) stands as a prime candidate for biodegradable implants and devices [12–15] because it is naturally found in the human body. It plays essential roles in metabolic pathways as an enzyme catalyst [16,17], in cell structure and function [18,19], and in bone formation and growth by promoting calcium deposition [20,21]. Although Mg is a highly electrochemically active anodic metal [13], advances in metallurgical alloy processing via phase design [13,22] and heat treatment [23] have opened avenues to address the rapid corrosion of Mg in order to meet clinical requirements. Additionally, metallurgical alloy design and processing of Mg alloys for biomedical applications have also enabled a variety of corrosion rates suitable for a wide range of biomedical applications. For example, the addition of Sr increases the corrosion resistance of Mg–Sr binary alloys [24].

Furthermore, previous in vitro studies showed that the degradation of Sr-containing Mg alloys sustained a stable and continuous release of Sr ions into the culture media which has potential implications for bone implant devices [24,25]. In the present study, we combine the well-known osteogenic properties of strontium with magnesium to generate a bioabsorbable implant material with stable Sr release after implantation, while tailoring the alloy's biocompatibility and degradation performance. Our previous research showed that addition of Sr in ternary Mg alloys improved the mechanical and corrosion properties [24,26], and addition of 1 wt.% Sr resulted in improved cytocompatibility with human embryonic stem cells when compared with 0.15, 0.5, and 1.5 wt.% Sr [25,26]. Therefore, the Mg–1Sr alloy (wt.%; designated in this study as J1 alloy per ASTM B275 standard [27] was chosen for the present in vivo study due to its suitable degradable, cytocompatible and mechanical properties [24,26]. Furthermore, a solution and aging treatment was investigated to optimize the microstructure and degradation properties of the J1 alloy by tailoring the microstructure and distribution of second phases as shown extensively for other Mg alloys [13,28].

The objectives of this work were to quantify the in vivo degradation rate, new bone formation and Sr ionic release of the heat treated J1 alloy, and evaluate the biocompatibility and changes in metabolic activity in response to the degradation following 16 weeks implantation into the mid-diaphysis of femora of New Zealand white rabbits. Based on these results, the long-term biocompatibility, metabolism and osteogenic activity of the J1 alloy and the suitability of the alloy as a bone implant material was shown.

2 Materials and Methods

2.1 Material preparation and characterization

The J1 alloy had a nominal composition of 1 wt.% Sr in Mg matrix. The chemical composition of the alloy was analyzed using an inductively coupled plasma-optical emission spectrometer (ICP-OES; VARIAN, Palo Alto, USA). The alloy was produced by a metallurgical process consisting of melting, casting, rolling, and heat treatment. A Mg-10 wt.% Sr master alloy (Norsk Hydro, Raufoss, Norway) was added to the high-purity Mg (99.99%; Magnesium Elektron, Manchester, UK) melt at 720 °C in nominal amounts under a protective atmosphere (Ar + 2% SF_6, flow rate = 6 L/min). After the melting process, the alloy was held at 710 °C for 30 min and cast as ingots at 720 °C. The ingots were air-cooled and rolled at 380 °C into 10.0 mm thick sheets with reduction rate of 50% prior to heat treatment which was a combination of solution treatment and aging. Solution treatment was carried out at 455 °C for 8 h followed by water quenching, and aging treatment was performed at 190 °C for 11 groups of samples from 30 h up to 330 h followed by water cooling.

The heat-treated specimens were mechanically polished using silicon carbide paper up to 3000 grit. A Zeiss Ultra 55 (Carl Zeiss GmbH, Oberkochen, Germany) scanning electron microscopy (SEM), operating at 15 kV, and equipped with an energy dispersive X-ray spectroscopy (EDS; EDAX International, Mahwah, USA) detector was used to observe the microstructure and analyze surface elemental compositions, respectively.

X-ray diffraction (XRD) measurements were also employed for the phase analysis, equipped with a diffractometer (Siemens D5000, Germany) with Cu Kα1 radiation (wavelength k = 0.15406 nm) and a secondary monochromator. The step size was 0.02 mm, and the time at each step was 3 s.

In preparation for high-resolution transmission electron microscopy (HR-TEM) analysis, the polished specimens were thinned by ion sputtering and observed using a Tecnai G2 (FEI Company, Eindhoven, The Netherlands) at 200 kV for phase identification.

Hardness measurements were carried out using a Vickers hardness test machine (FM800, Future-Tech Company, Kawasaki, Japan) with a load of 5 kg and a dwelling time of 10 s. A mean value of 15 measurements was used for each test condition.

2.2 In vitro cytocompatibility and hemocompatiblity

Primary human osteoblasts were cultured from cancellous bone chips obtained from patients undergoing total hip arthroplasty following patient consent. The cancellous bone was cut into pieces, and after removal of bone marrow, the bone chips were cultured in Dulbecco's Modified Eagle Medium (DMEM; Sigma Aldrich Chemie, Taufkirchen, Germany) with the addition of 15 v/v% fetal bovine serum (FBS; PAA Laboratories, Linz, Austria). The culture was maintained for approximately 10 days without medium change. Thereafter, the medium was changed every three days and cells were passaged after reaching 80% confluency.

To evaluate the cytocompatibility of the J1 alloy, osteoblasts were seeded at a density of 1 x 10^4 cells per ml of media and cultured on the surfaces of the cell-culture treated well-plates (positive control), pure Mg, and J1 alloy in DMEM + 15% FBS. Cell culture medium was changed every 48 h and the total incubation time was 21 days. Cell viability was then determined using a Viability/Cytotoxicity Kit (Invitrogen, Karlsruhe, Germany), which measures the cellular membrane integrity following the manufacturer's instructions. A fluorescence microscope (Eclipse Ti-S, Nikon, Düsseldorf, Germany) was utilized to observe and calculate the viability of tested cells.

Hemolysis test was performed according to ISO 10993.4 standard [29]. Healthy human blood was collected from a volunteer, and diluted with isotonic saline solution (Sigma–Aldrich, Shanghai, China) to 0.9% by volume. Samples of the J1 alloy and pure Mg control were placed in sterile centrifuge tubes with 10 ml of the diluted blood and incubated for 60 min at 37 °C. Saline solution without blood was used a negative control and TritonX-100 solution (Yuanmu, Shanghai, China) as a positive control. Subsequently, all the tubes were centrifuged (4000 rpm, 3 min), the supernatant was carefully removed and transferred to a cuvette, and finally analyzed using an ultraviolet spectrophotometer (7200, UNIC, USA) to determine the optical density (OD) at 545 nm to measure hemoglobin content. The extent of hemolysis was calculated based on the average of five triplicates according to the following equation [30]:

$$Hemolysis(\%) = \frac{OD(test) - OD(negativecontrol)}{OD(positivecontrol) - OD(negativecontrol)} x100\% \quad (1)$$

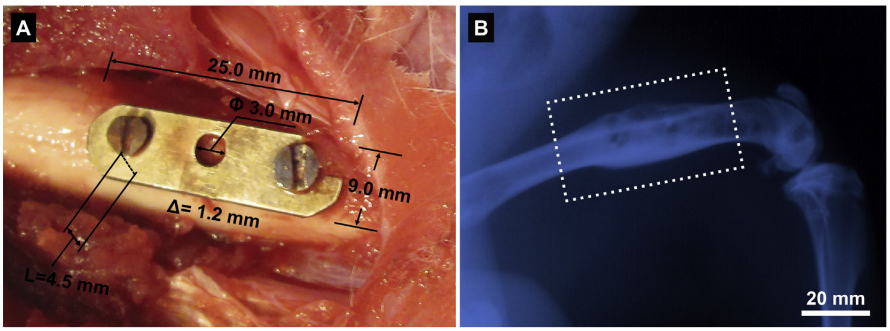

Figure 1: Intraoperative appearance of the femur and the implant device, where U responds to diameter and D responds to thickness (A). Radiographs of the implantation site at 1 week after surgery (indicated by the frame, B).

2.3 Animals and surgical procedure

The implant device was composed by a plate and two screws, and machined by a numerically controlled versatile lathe (Junker, Nordrach, Germany). The size and layout of the implant, and surgery site are depicted in Fig. 1A. All procedures in the present study were performed in full compliance with the institutional and protection laws and approved by the local animal welfare committee (The State scientific and technological commission of China) [31].

To test alloy implants similar to real implant devices used in human body in size, New Zealand White Rabbit as a standard laboratory animal was chosen for in vivo tests [32]. Female New Zealand White rabbits (SYAU, Shenyang, China), 6–8 weeks of age, were randomly assigned to three groups: J1 alloy implantation group (n = 6), pure Mg implantation group (n = 6) and sham operated group control (n = 6).

Prior to the surgical procedure the implants were sterilized by gamma irradiation. The fixation plate was placed parallel to the longitudinal axis of the femur and the screws were inserted perpendicular to this axis and bicortically across the diaphysis as shown in Fig. 1A. During the drilling procedure the area was flushed with an isotonic saline solution and the implant was then press-fit inserted. The wounds were then carefully sutured and following the surgery all animals were administered post-op meds and kept for 16 weeks in stainless steel cages with controlled environment (temperature: 22 °C; humidity: 60% and light: 12 h light/dark cycle) and sterile paddy husk as bedding in ventilated animal rooms. Water and food (SYAU, Shenyang, China) were available to the animals ad libitum.

2.4 In vivo degradation behaviors

The implants were collected and washed by chloride acid to remove surface adherent bone and other tissues after 1 week (1w), 4w, 8w, 12w and 16w post-implantation in triplicate for degradation analysis. The sample surface post-implantation was observed and the surface elemental composition was analyzed using SEM and EDS, respectively. Three-dimensional (3D) reconstructions of the surface post-implantation were generated using Avizo 3D software (FEI Company, Eindhoven, The Netherlands).

The corrosion potential of the test materials in blood plasma was measured using a potentiostat (Parstat, Princeton Applied Research, Oak Ridge, USA). A saturated calomel electrode (SCE, E0 = 0.241 V vs. SHE – standard hydrogen electrode) was used as reference electrode, and all measurements were performed at room temperature.

Furthermore, the chemical composition of the species present in the corrosion layer were identified using X-ray induced photoelectron spectroscopy (XPS) using a Kratos Axis Ultra DLD (Kratos Analytical Ltd., Manchester, UK) attached with a 15 kV X-ray gun using monochromatic Al Kα radiation. The spot size was 700 μm x 300 μlm and the pass energy was 40 eV at the measured regions and 160 eV for survey scans.

Additionally, Mg 2p core energy levels from XPS survey spectra were analyzed and the binding energy (binding energy database NIST Standard Reference Database 20, Version 3.5) for Mg compounds was determined (accuracy of $\pm$ 0.3 eV). The curve fitting for chemical composition was performed with Casa 2.3.15 software (Casa Software Ltd., Teighnmouth, Devon, UK). Subsequently, the corrosion layer on the implants were then removed by immersion in chromic acid (180 g L^{-1}) for 10 min to determine net mass. The average corrosion rate (CR) was calculated in millimeters per year (mm y^{-1}) using the following equation [37]:

$$CR = \frac{\Delta V}{A \cdot tNenner} \tag{2}$$

In the equation, CR is Corrosion rate (mm y^{-1}); DV is Volume loss (mm^3); A is surface area (mm^2); t is Corrosion time (y).

2.5 In vivo biocompatibility

2.5.1 Histopathological observation

Vastus lateralis muscle close to the implantation site, spleen, kidney and liver harvested from the test animals 16 week post implantation were fixed in 10% formalin, embedded in paraffin, sectioned, and stained with hematoxylin and eosin

(H/E) for histological examination using standard techniques [33]. After H/E staining, the slides were observed and photos were taken using an optical microscope (Olympus X71, Japan). The fixed sections were then inspected through routine pathology in a blind randomized fashion.

2.5.2 Hematology analysis

Approximately 1.0 mL of blood was drawn and collected every week during the culture in potassium EDTA tubes using a standard saphenous vein blood collection technique for hematology analyses. The collection tubes were centrifuged twice at 3000 rpm for 10 min in order to fraction the blood. The serum was collected and six standard hematology markers were analyzed: red blood cell count, white blood cell count, platelet count, hemoglobin, hematocrit and mean corpuscular volume (MCV). All hematology markers were analyzed using a Biochemical Autoanalyzer (Type 7170, Hitachi, Japan).

2.5.3 Cardiac damage, inflammation, and liver function assays

For a more comprehensive determination of the biological effects in response to biomaterial corrosion, the concentrations in albumin (ALB) and the serum of lactate dehydrogenase (LDH) were measured every 4 weeks along with the blood test. ALB, which is generally regarded as a "negative" acute-phase protein is commonly downregulated during inflammation and was therefore used as a marker of inflammation [34]. LDH is a highly specific marker that is elevated in the blood for several days following cardiac damage and was therefore used as an indicator of cardiac damage [35]. Furthermore, liver function was evaluated every 2 weeks using serum concentrations of total bilirubin levels (TBIL), alanine aminotransferase (ALT), and aspartate aminotransferase (AST). TBIL, ALT, and AST are important markers of liver function because upregulation of these markers means impaired liver function [36].

2.6 Metabolic process

To measure the concentration of Sr^{2+} in organs, the entire kidney, liver and spleen of the animals were harvested in triplicate at 4w, 8w, 12w, and 16w post-implantation. The wet samples were weighed, digested with nitric acid (60 v/v%, Sigma, USA) by heating and then analyzed for Sr^{2+} concentration by ICP-OES analysis. Using the same method, the test animals' blood plasma was collected and analyzed biweekly post implantation to measure Sr^{2+} and Mg^{2+} ion concentration.

2.7 Osteogenic activity of the J1 alloy

2.7.1 Histological evaluation

The bone samples with implants were harvested after 16 weeks implantation and fixed in 10% buffered formalin for 72 h. Subsequently, the samples were serially dehydrated in increasing ethanol (70 v/v%, 95 v/v%, 100 v/v%; 72 h for each step). Finally, the calcified tissue and implants were embedded in methylmethacrylate (Technovit 9100 New®, Heraeus Kulzer, Hanau, Germany) following the manufacturer's instructions. The embedded samples were then cut and grounded into sections with a thickness of approx. 50 μm. The sectioned samples were stained with Giemsa stain (MERCK, Germany) following the manufacturer's instructions.

The stained sections were observed using light microscopy to conduct the morphological and histological evaluations. Specifically, bone in-growth and direct bone-implant contact was quantified to determine osteointegration of the implant [11]. Bone ingrowth was calculated by the percentage of new bone formation within the standard area, while the bone-to-implant contact was determined by using the side of the reference area located along the implant. Subsequently, the length of the areas with direct contact between implant and new bone was measured and the data expressed as the percentage of direct contacts with respect to the side of the reference area.

2.7.2 Osteogenic gene analysis

The section around implantation site (length = 55 mm, as shown in Fig. 1B) of left femora was obtained 16 weeks after operation from each test animal (six animals for each test material). RNA was isolated from the bone tissue around the implantation site with the FastTrack MAG mRNA Isolation Kit (Invitrogen, Carlsbad, US) according to its protocol, and RNA quality and quantity was determined by a Qubit fluorometer (Invitrogen, Carlsbad, US). 1.0 mg of RNA was reverse-transcribed to cDNA with the Superscript Kit (Invitrogen, Carlsbad, US) as described in the manufacturer's protocol. The expressions of the selected genes include: runt-related transcription factor 2 (Runx2), alkaline phosphatase (ALP), osteocalcin (OCN) and collagen, type I, alpha 1 (Col1a1), which were quantified by Quantitative polymerase chain reaction (qPCR, MJ Research, Edgewood, Canada) in combination with SYBR Green PCR Master Mix (Applied Biosystems, Foster City, US) according to the manufacturer's protocol.

Samples were processed without reverse transcription to control for contamination with genomic DNA and RT-PCR runs without template as controls. The relative mRNA expression level of each gene was normalized with the reference gene β2-microglobulin (B2 M, Sino Biological, Beijing, China) and determined

by the Cycle threshold (Ct) values. The relative gene expression ratio for each gene was calculated by the PCR efficiency (E) and Ct value of a sample compared with the control using REST software (REST 2009, Technical University Munich, Munich, Germany), and expressed in comparison to the reference gene according to Pfaff's model [37]:

$$Expression\ ratio = \frac{(E_{target})\Delta Ct_{target}(control - target)}{(E_{ref})\Delta Ct(control - sample)} \quad (3)$$

2.7.3 Local delivery of Sr content

The morphology and distribution of Sr content on the surrounding bone tissue after 16 weeks implantation was investigated by SEM and ICP-OES. For electron microscopy, bone tissue close to implant area was excised and immediately fixed in 3% glutaraldehyde overnight at 16 week post implantation. Then the samples were treated according to the general protocols for SEM study at 18 kV [38]. Distribution of Sr content in bone tissue around the implantation site was determinated by ICP-OES analysis.

2.8 Statistical analysis

All in vitro experiments were carried out in five-duplicates. For the in vivo experiments, each group (J1 group, pure Mg group and sham control) was composed of six animals for entire 16w implantation, plus three animals for every single time point in degradation and metabolism test prior to the 16w time point (1w, 4w, 8w and 12w post implantation) as described in the experimental procedures. Results were expressed as mean $\pm$ standard deviation (SD). Gene expression was analyzed by REST software and presented as box plots. Multi-group comparisons of the means were carried out by one-way analysis of variance (ANOVA) test using SPSS 14.0 (SPSS Inc., Chicago, USA) with confidence intervals of 95% and 99% indicated by *$p < 0.05$ and **$p < 0.01$ (or $^{\dagger\dagger}p < 0.01$), respectively.

3 Results

3.1 Microstructure characterization

The experimentally measured composition of J1 alloy was: Sr 1.03 $\pm$ 0.01 wt.% and balanced Mg. Impurities mainly composed by Ni (<0.003 wt.%), Fe (<0.002 wt.%) and Cu (<0.002 wt.%). The loss of alloying elements was 0.03 wt.% Mg by surface oxidation during melting process.

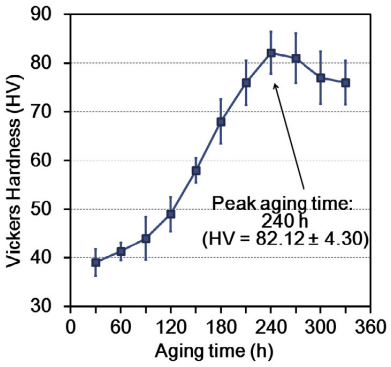

Figure 2: Age hardening response of the J1 alloy at 190 °C. The experiments were carried out in ?fteen-duplicates and mean value ± standard deviation is presented.

The Vickers hardness of the J1 alloy was measured after aging between 30–330 h with 30 h increments at 190 °C and results are shown in Fig. 2. The age-hardening response is significant for J1 alloy, whose peak hardness (82.12 ± 4.30 HV) is obtained after 240 h aging (Fig. 2), and further ageing led to a slow decrease in the hardness. A consistent increase in hardness was observed up to a maximum (82.12 ± 4.30 HV) obtained after 240 h of aging time. Thereafter, the hardness decreased and hit a plateau at approx. 76.0 ± 4.5 HV. Therefore, 240 h was selected as the aging time for the J1 alloy. Compared with pure magnesium (27.8 ± 0.8 HV, measured in the same conditions), the addition of strontium resulted in a significant increase (over 190%) in the peak hardness, which was attributed to precipitation hardening brought by re-precipitation of $Mg_{17}Sr_2$ β phases during aging treatment.

Fig. 3A shows the SEM micrograph of the J1 alloy which indicated that the microstructure of the heat treated alloy consisted of an α-Mg matrix with precipitates distributed along grain boundaries, which had a composition similar to $Mg_{17}Sr_2$ and the phases were identified by XRD analysis (Fig. 3B). Fig. 3C presents HR-TEM micrographs of the re-precipitated $Mg_{17}Sr_2$ phase by aging treatment and corresponding diffraction pattern for the heat treated J1 alloy, which dispersed inside grains and their average diameter were ca. 5 nm. The reflections in the diffraction pattern can be indexed according to the metastable secondary phase, which had a base-centered orthorhombic structure [39,40].

3.2 In vitro cytocompatibility and hemocompatibility

Results for osteoblast viability at the conclusion of the 21-day cytocompatibility experiments are summarized in Fig. 4. Fig. 4A–C show fluorescent images of

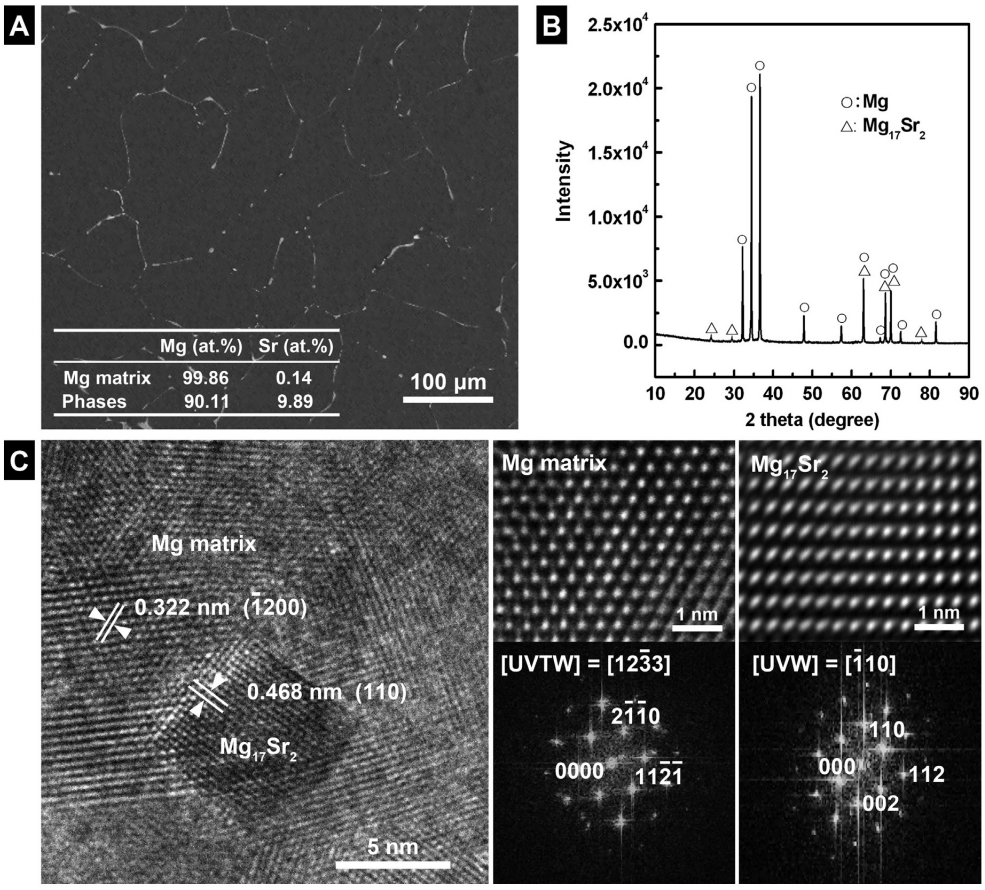

Figure 3: EM microstructure of the aging treated J1 alloy with EDS analysis results (A). XRD pattern of the aging treated J1 alloy (B). HR-TEM micrograph showing the reprecipitates distribution and the corresponding diffraction patterns of the J1 alloy in peak-aged condition (C). $Mg^{17}Sr_2$ second phase was identi?ed by XRD and HR-TEM analysis. Re-precipitates (ca. 5 nm) generated during aging treatment dispersed inside grains while coarser-sized precipitates (ca. 2–10 μm) obtained in the cast condition distributed along grain boundaries.

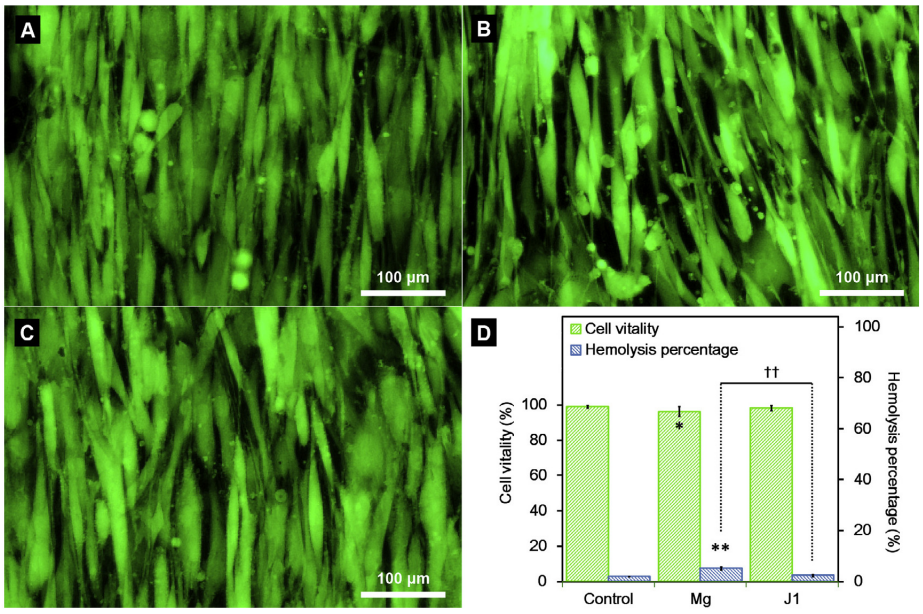

Figure 4: Fluorescent microscope images of human osteoblasts after 21 days incubation on the well-plate (A), pure magnesium (B) and the J1 alloy (C), where living cells were stained green and dead cells red. The survival rates of human osteoblasts after 21 days incubation on the J1 alloy, and qualitative evaluation of hemolysis of the J1 alloy (D). The experiments were carried out in ?ve-duplicates and mean value $\pm$ standard deviation is presented. Signi?cant differences compared with control are marked with *($P < 0.05$) and **($P < 0.01$), and signi?cant differences between pure Mg and J1 alloy are marked with ††($P < 0.01$).

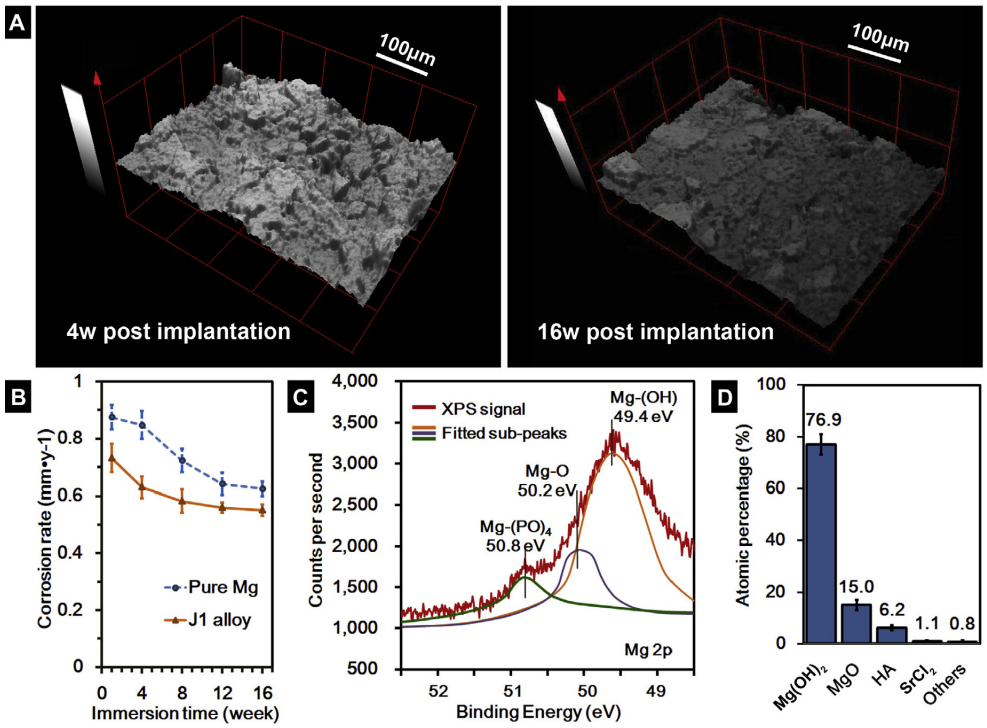

Figure 5: 3D reconstructions of the implant surface based on SEM images (A). Corrosion rate of the implant calculated by weight loss (B). XPS spectra of Mg 2p core energy levels for the corrosion layer of the J1 alloy at 16w post-implantation (C). Compositions of corrosion products in the J1 alloy at 16w post-implantation derived from XPS analysis (D).

osteoblasts adhered directly onto the surfaces of the well plates, pure Mg control, and J1 alloy. Cell viability was quantified and percent viability is summarized in the histogram in Fig. 4D. These results showed a mean percent viability of 98.3 $\pm$ 1.5% and 96.3 $\pm$ 2.7% for the cells grown on the J1 alloy and on pure magnesium, respectively.

Similarly, results for hemolysis results after the 20 min incubation in diluted human blood are summarized in Fig. 4D. The results showed that the J1 induced a 2.54% hemolysis compared with 7.13% for the pure Mg control. The cell adhesion and hemolysis results indicated that J1 is more cytocompatible than pure magnesium, which is widely considered as biocompatible and non-toxic implant material.

3.3 Clinical observations and in vivo degradation process

All the animals in test and control groups survived the entire observation period. Clinical healing of the surgical wounds and complete recovery of mobility of all animals progressed with no visible adverse effects until the end of the observation period (16w post-implantation). Fig. 5 summarizes results for the in vivo corrosion assessment of the implant. Fig. 5A shows 3-D renderings of SEM micrographs on the surface of the J1 alloy 4w and 16w post-implantation. These images showed that localized corrosion occurred on the surface but the dominant corrosion type was homogeneous corrosion. A qualitative analysis of the surface topography indicated that the surface of the implant became less rough with longer implantation time possibly due to the reduced localized corrosion caused by the thickening corrosion layer.

Fig. 5B shows the corrosion rate of alloys after implantation for 1, 4, 8, 12 and 16w calculated from implant mass loss. The corrosion rate of the J1 alloy decreased from 0.73 ± 0.05 mm y^{-1} at 1w to 0.62 ± 0.04 mm y^{-1} at 4w and 0.55 ± 0.03 mm y^{-1} by 16w. In contrast, the pure Mg control had a significantly higher corrosion rate ($p < 0.001$) compared with the J1 alloy during all time points evaluated; specifically, the largest difference was observed at 4w with a value of 0.85 ± 0.04 mm y^{-1}. Significant lower in vivo corrosion rate of the J1 alloy was attributed to the cathodic shift in standard electrode potential, which was -1.0 V vs. SHE for the J1 alloy compared with -1.5 V vs. SHE for pure Mg in blood plasma. In order to better understand the corrosion behavior of the materials under physiological conditions a detailed composition analysis of the corrosion layer of the J1 alloy was performed by XPS analysis after 16 weeks implantation. A detailed analysis of the Mg 2p spectra (Fig. 5C) was carried out to identify distinct Mg binding energies and compounds. The Mg 2p spectra stretched out from 47.0 eV to 52.8 eV [41]. The broadening of the peak was deconvoluted and fitted with $Mg(OH)_2$at 49.4 eV, MgO at 50.2 eV and Mg–PO_4 at 50.8 [42].

Furthermore, compounds present in the corrosion layer of the J1 alloy at 16w were calculated by XPS signal integration and the atomic percent of each component is plotted in the histogram in Fig. 5D. These results showed that the corrosion layer was largely composed of $Mg(OH)_2$, MgO, and hydroxyapatite (HA), and contained small amounts of $SrCl_2$ and other compounds.

3.4 Histopathological observation

To obtain a comprehensive toxicity assessment induced by the Mg-based samples at 16w post-implantation, histological evaluation was performed on collected samples of: the vastus lateralis muscle to assess peri-implant localized toxicity; and the spleen, kidney and liver to assess systemic toxicity. Specifically, histolog-

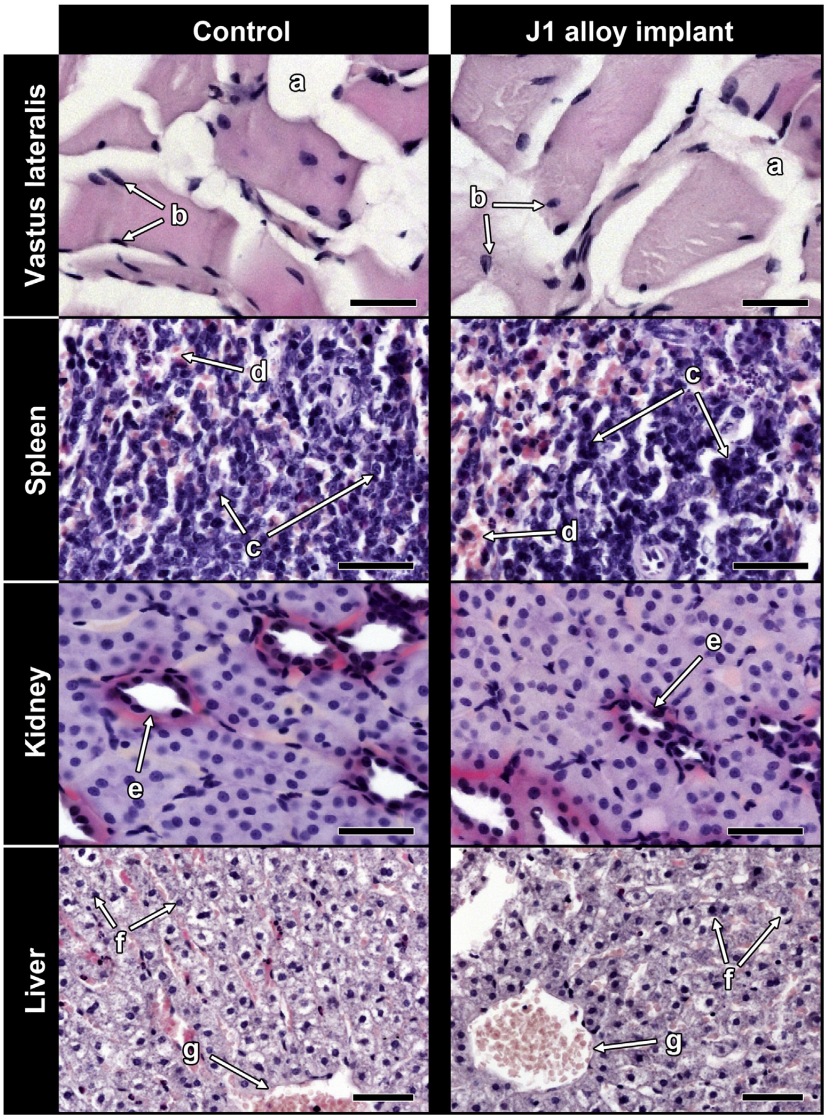

Figure 6: H&E-stained tissue sections from sham control and test animals at 16w after implantation of J1 alloy. Data are representative of six test animals. Tissues were harvested from Vastus lateralis (the muscle close to the implantation site), spleen, liver and kidney, with 'a' representing endomysium, 'b' representing nucleus, 'c' representing the T-cells in periarteriolar lymphoid sheath, 'd' representing red pulp, 'e' representing proximal convoluted tubule, 'f' representing hepatocytes, and 'g' representing hepatic portal area. The scale bar is 500 μm.

ical evaluation focused on tissue damage, inflammation, and lesions from toxic exposure. Optical images of the H/E stained tissue sections of the organs from animals with the J1 implants at 16w post-implantation are shown in Fig. 6.

Qualitative evaluation of all tissue sections showed similar cellular structures for the J1 group compared with the sham control and an absence of necrotic tissue in both groups. Furthermore, tissue from the vastus lateralis showed neither hydropic degeneration nor evident morphological changes in the nuclei and endomysium. Similarly, evaluation of red pulp and the T-cells in periarteriolar lymphoid sheath found in the spleen sections showed no structural or pathological changes such as hyperplasia. Analysis of the kidney tissue showed normal and easily identifiable proximal convoluted tubule structures in both J1 and control groups. Lastly, hepatocytes as well as hepatic portal areas in the liver samples appeared normal and there were no inflammatory infiltrates.

3.5 Hematological, inflammation, cardiac, and hepatic systemic responses

Results from the biochemical analyses used to measure hematological, inflammation, and cardiac function indices are summarized in Fig. 7. Results for all six hematological serum indices (Fig. 7A) showed no significant changes in the J1 group at 16w post-implantation compared with the control. Additionally, serum concentrations of ALB and LDH were used as indices of systemic inflammation and cardiac function, respectively, and results are shown in Fig. 7B and C, respectively. These results showed that the mean ALB concentrations for the Mg control group were significantly lower when compared with the J1 group for all time points. LDH concentrations for the Mg control group were significantly higher when compared with the J1 group when implantation time exceeded 4 weeks. In contrast, the ALB and LDH concentrations at 16w post-implantation for the J1 group did change compared to the baseline levels measured pre-implantation (0w).

Results from the biochemical analyses used to measure hepatic functions are summarized in Fig. 8. Serum concentrations of ALT, AST, and TBIL were all elevated post-implantation for the J1 and pure Mg groups up to approximately 8–10w post-implantation (Fig. 8A). Thereafter, the concentrations of all three indices returned to normal physiological pre-implantation (0w) values. Consistently, values for all three indices of the Mg group were higher compared with the J1 group. Specifically, the highest TBIL concentration was measured for the Mg group at 6w (1.63 ± 0.151 μM), and the highest ALT and AST concentrations were both measured for the Mg group at 2w (73.0 ± 5.11 IU L^{-1} and 179 ± 10.7 IU L^{-1}, respectively), when the highest corrosion rate of the implant was observed (Fig.

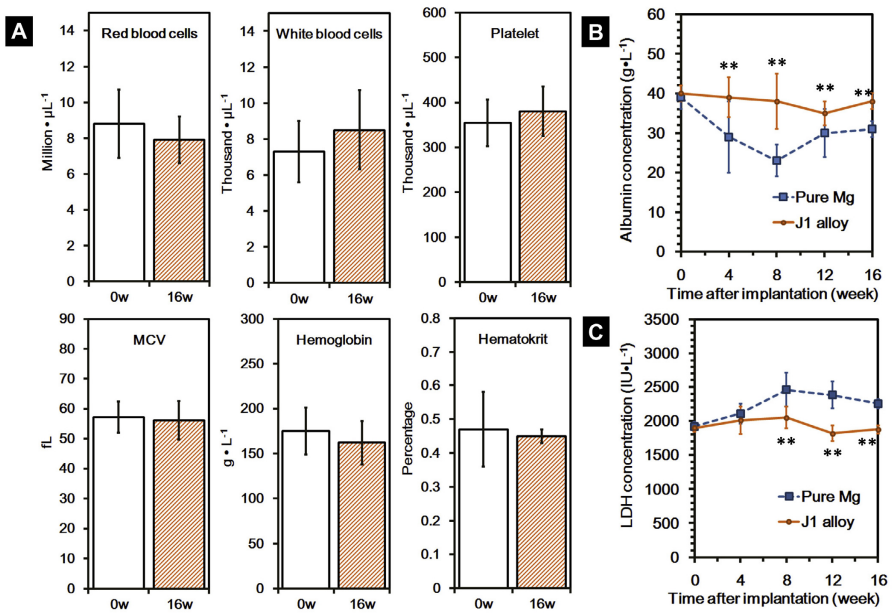

Figure 7: Six hematological serum indices of the test animals before and after implantation of J1 alloy (A), serum concentrations of albumin (B) and LDH (C) of the test animals post-implantation. ALB is downregulated during in?ammation while LDH is elevated following cardiac damage. The experiments were carried out in six-duplicates and mean value ± standard deviation is presented. Signi?cant differences between pure Mg group and J1 alloy group are marked with **(P < 0.01).

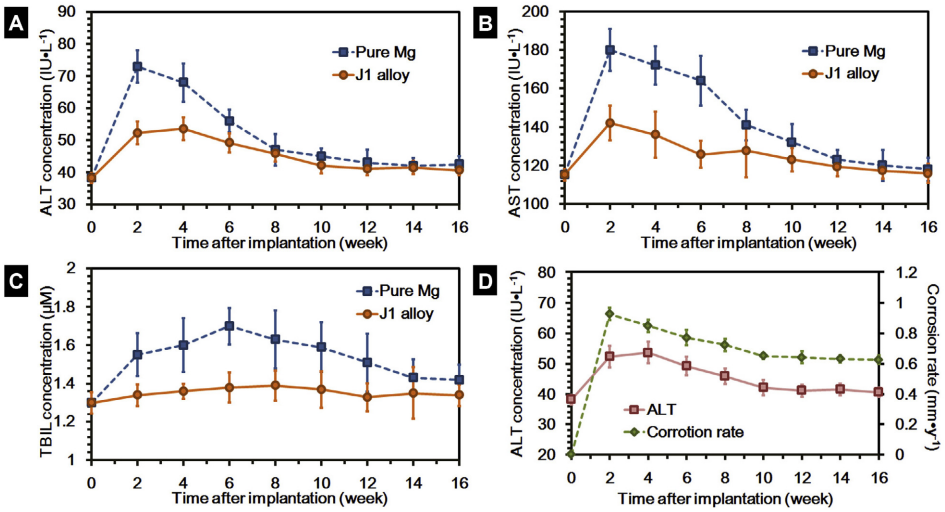

Figure 8: Serum concentrations of ALT (A), AST (B), and TBIL (C) of the test animals as primary indices of liver function, and comparison of corrosion rate of the J1 alloy implant and serum ALT concentration (D). Upregulation of TBIL, ALT, and AST means impaired liver function. The experiments were carried out in six-duplicates and mean value ± standard deviation is presented. Signi?cant differences are marked with *($P < 0.05$).

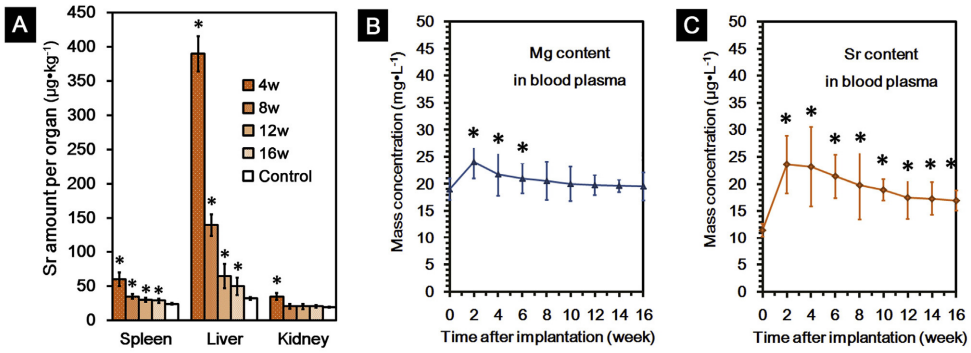

Figure 9: Sr contents in spleen, liver and kidney (A) and metabolic process of Mg (B) and Sr (C) ions in blood plasma of the test animals after implantation of J1 alloy. The experiments were carried out in six-duplicates and mean value $\pm$ standard deviation is presented. Signi?cant differences compared with sham control group are marked with *($P < 0.05$).

8D). Taken together, the histological qualitative evaluation and the biochemical quantitative evaluation at 16w post-implantation with the J1 implant showed no adverse effects on hepatic functions.

3.6 Metabolism of Mg^{2+} and Sr^{2+} ions

Fig. 9 summarizes the mean ionic content in tissues of interest (spleen, liver, and kidney) and in the blood plasma of the J1 group at prescribed time intervals during the 16w study. The estimated average half-life periods of Sr^{2+} ion in spleen, liver and kidney of the test animals were 12w – 16w, less than 4w and 12w – 16w respectively. These results showed that Sr^{2+} content was increased in all three organs compared with the control at 4w postimplantation. The highest increase of Sr^{2+} content was measured for the liver (388 ± 25 μg kg^{-1}) at 4w post-implantation and returned to 32 ± 2 μg kg^{-1} after 16w implantation. Normal Sr^{2+} content in the spleen and liver were recovered at 8w; in contrast, slightly elevated Sr^{2+} content in the liver was measured up to 16w post-implantation. Ionic concentrations of $Mg^{2+}$and Sr^{2+} in the blood plasma of the J1 group during the 16w study are summarized in Fig. 9B and C, respectively. These results showed a slight systemic increase in both Mg^{2+} and Sr^{2+} at 2w as a result from the degradation of the J1 implant. Baseline plasma concentration of Mg^{2+} was recovered at approximately 4w post-implantation (24.3 ± 3.3 mg L^{-1}, Fig. 9B) whereas Sr^{2+} plasma concentration remained slightly elevated at 16w post-implantation (16.9 ± 1.8 μg L^{-1}, Fig. 9C). Collectively, these results indicated that Mg^{2+} ions were metabolized with great efficiency and even with an almost threefold increase

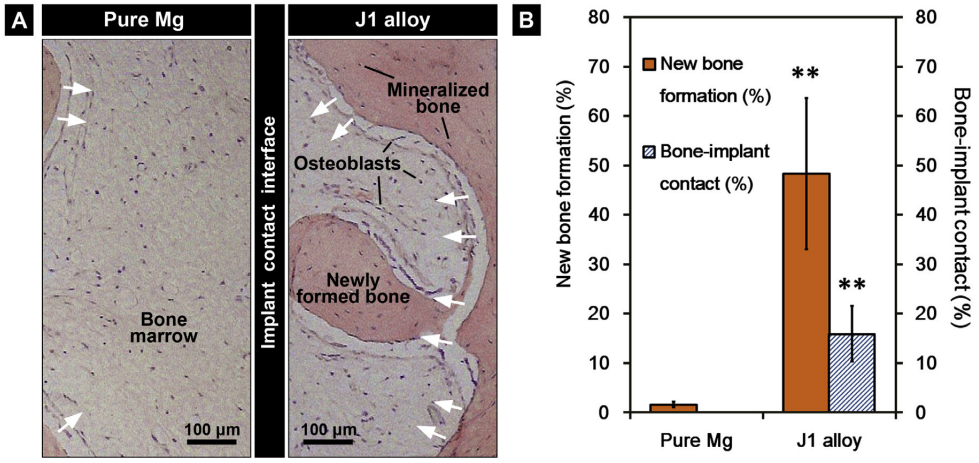

Figure 10: Comparison between the two representative cortical/trabecular interfaces in surrounding bone tissue response to pure Mg control and J1 alloy after 16w of implantation, where new bone ingrowth (white arrows) was observed to form towards the implant interface (A). The area of new bone formation inside the box was measured for all six samples to calculate the percentage of new bone formation with respect to the total reference area. Percentage of new bone formation and percentage of direct bone-to-implant contact were summarized (B). Mean value $\pm$ standard deviation is presented and signi?cant differences between pure Mg group and the J1 alloy are marked with **($P < 0.01$).

in Sr^{2+} content in the liver and blood plasma, excess Sr^{2+} was metabolized and excreted and near-homeostatic values recovered.

3.7 Osteogenic activity of the J1 alloy

Fig. 10 shows the cortical/trabecular interface in surrounding bone tissue response to both pure Mg control and J1 alloy after 16w of implantation, where new bone ingrowth (white arrows) was observed to form towards the implant interface. J1 alloy implant showed direct contact with the newly formed bone, whilst no direct contact between pure Mg implant and bone was found. Osteoblasts, which are responsible for new bone formation, were also observed around the implants (Fig. 10A). Quantified results of new bone formation and bone-implant contact rate were summarized in Fig. 10B.

Fig. 10 summarizes the osseointegration analysis of the J1 and Mg implants at 16w post-implantation. Representative Giemsa-stained undecalcified MMA sections of the bone-implant interface for both groups are shown in Fig. 10A. In these images dark-pink regions stain calcified tissue, light-purple stains bone marrow

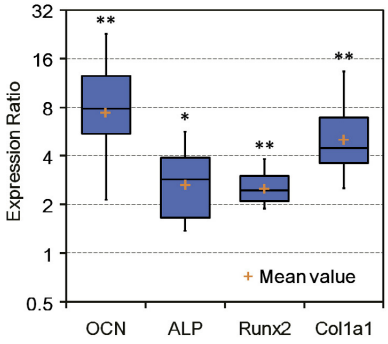

Figure 11: A representative morphology by SEM of the surrounding bone tissue after 16 weeks J1 alloy implantation with EDS analysis result to the distribution of Sr content. The concentration of Sr content was measured in all six samples, and mean value ± standard deviation is presented.

cells, and dark-purple stains cell nuclei. Qualitatively, these images showed increased new bone formation (NBF) around the J1 implant compared with the Mg control. Further analysis showed that the J1 implant had direct bone-to-implant contact (BIC) with the de novo bone observed; in contrast, the pure Mg control implant did not show any BIC. Quantification of NBF and BIC showed statistically significantly higher values ($p < 0.01$) for the J1 group (48.3% ± 15.3% and 15.9% ± 5.6%, for NBF and BIC respectively) compared with the Mg control group (1.6% ± 0.5% and 0, for NBF and BIC respectively).

Fig. 11 depicts expression differences of the selected genes determined by qPCR between the J1 alloy and pure Mg groups normalized to B2 M gene expression. OCN expression analysis indicates a significant higher osteocalcin expression in the J1 alloy group when compared to the pure Mg group ($p < 0.01$). Expression of ALP as an osteoblast marker indicating mineralization of bone was significant higher in the J1 alloy group compared with the pure Mg group ($p < 0.05$). Expression level of Runx2 (a key transcript factor for bone formation) and Col1a1 (main content of bone extracellular matrix) also showed significant difference ($p < 0.01$) between the J1 alloy and the pure Mg group.

Fig. 12 shows the morphology of the surrounding bone tissue after 16 weeks J1 alloy implantation with EDS analysis result to the distribution of Sr content. There is experimental evidence thatthe Sr element permeated through the bone tissue from the boneimplant interface. Distribution of Sr content could be estimated by fitting the logarithmic diffusion equation [43] to the curve (as shown in Fig. 12):

$$C = -7.45ln(d) + 1.76x10^{-2}d + 58.5 \quad (4)$$

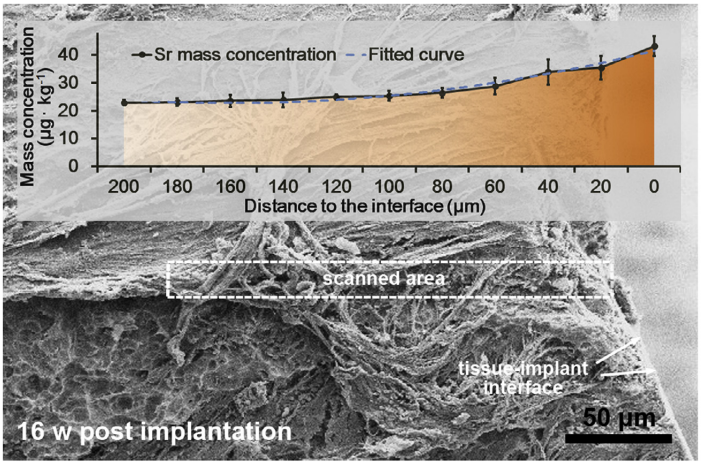

Figure 12: Relative gene expression analysis between pure Mg group and the J1 alloy group, with OCN, ALP, Runx2 and Col1a1 as bone formation markers. B2 M was used asa reference gene. The experiments were carried out in six-duplicates and presented as box plots. Signi?cant differences are marked with *($P < 0.05$) and **($P < 0.01$).

C (μg kg^{-1}) is concentration of Sr content, and d (μm, d $\geq$ 10.0 μm) is the distance to the implant-bone contact; mean square error = 4.8%] The distribution of Sr content was primarily in logarithmic decrement, which hinted Sr ion was mainly transported by passive transportation and controlled by osteal cellular processes [43].

4 Discussion

The age-hardening response was significant for J1 alloy (Fig. 2) due to the low solubility of Sr in Mg (0.11 wt.% at the eutectic temperature 585 °C [40] and the corresponding tendency for reprecipitation of Sr at the grain boundaries rather than dispersion in the α-Mg matrix [44]. It has been suggested that grain refinement induced by addition of Sr in excess of the solid solubility limit to Mg-alloys, is dictated by the grain growth restriction mechanism of secondary phase particles distributing on the advancing interface of the solid/liquid [25,45,46].

Additionally, during the aging treatment the $Mg_{17}Sr_2$ phase re-precipitated as fine particles (ca. 5 nm, Fig. 3C) compared with the coarser-sized particles (ca. 2– 10 μm) obtained in the as-cast condition (Fig. 3A). Due to this Sr induced precipitation-hardening effect, the Vickers hardness of the J1 alloy was improved with peak aging time achieving values nearly twice as high compared with cast

and solution treated alloys. Although the ageing treatment time and Vickers hardness of the age-treated J1 alloy was optimized, future studies will evaluate and optimize the compressive strength, fracture toughness, and elongation since these properties are of specific importance for orthopedic implant applications [12].

The in vivo corrosion rate of J1 alloy was found significantly lower compared with pure Mg for all time points evaluated during the 16w study (Fig. 5B).The significant lower in vivo corrosion rate of the J1 alloy is attributed to the cathodic shift in standard electrode potential caused by the addition of Sr to the α-Mg matrix, i.e. -1.0 V vs. SHE for the J1 alloy compared with -1.5 V vs. SHE for pure Mg when measured in blood plasma. Furthermore, the fine $Mg_{17}Sr_2$ particles obtained during aging were speculated to have played a role of inducing a homogeneous corrosion [47] on the surface of the J1 alloy as opposed to highly localized, pitting, and crevice corrosion reported for other Mg alloys [25,45,48]. As a result, at the conclusion of the 16w implantation, minor localized corrosion was observed on the surface of the J1 alloy (Fig. 5A), which is an important aspect to help reduce possible structural failures in clinical applications [49]. Structural failures induced by high corrosion rate may result in loss of mechanical integrity of the implant, which is also the primary limitation of Mg alloy implants used in the load bearing application [50].

Despite of suitable corrosion rate observed in the in vivo degradation experiment of J1 alloy implants compared with pure magnesium implants (Fig. 5), careful selection of Sr content in the Mg–Sr alloy is still an important consideration when applied as a load bearing material. Although the mechanical properties could be enhanced due to continued precipitation hardening, the amount of cathodic $Mg_{17}Sr_2$ intermetallic phases could accelerate corrosion by forming microgalvanic couples with the α-Mg matrix [51,52]. Furthermore, the adsorption of organic materials, such as proteins, into the corrosion layer has been reported to have a protective effect on the surface of Mg alloys [47,53]. It has been proposed that this composite corrosion film could significantly reduce the adsorption and diffusion of Cl^- ions across the corrosion interface [54] to reduce the corrosion rate. Lower corrosion rate also assures the alloy's cytocompatibility as well as hemocompatibility (Fig. 4D), based on which the in vivo biocompatibility of the J1 alloy could be mostly warranted.

The degradation of the J1 implant showed increased periimplant bone formation without any adverse effects, most likely due to the release of Sr^{2+} ions. In a similar study, Gu et al. implanted as-rolled Mg–2Sr pins into the distal marrow cavity of mice femora [25]. At the end of their 4w study, they observed a significant increase in bone mineral density, cortical bone thickness, and new bone formation compared with their sham control. However, the absence of a pure Mg control made it impossible to discern whether the increase in bone parameters was due to Mg^{2+} ions, Sr^{2+} ions, or both. Similar to the results from Gu et al., our

results showed an increase in positive parameters of osseointegration. In addition, our results showed that the Mg group was able to achieve only a small amount of NBF (1.6% $\pm$ 0.5%) with a faster corrosion rate (0.85 $\pm$ 0.04 mm y^{-1}, Fig. 5B). In contrast, the slower-degrading J1 alloy (0.73 $\pm$ 0.05 mm y^{-1}, Fig. 5B) achieved significant higher expressions of four osteogenesis related genes (Fig. 11) as well as a high amount of NBF (48.3% $\pm$ 15.3%) and a significant increase in BIC (15.9% $\pm$ 5.6%, Fig. 10B).

Although previous studies have shown that the human body can accommodate the effects of fast degrading implants [12,14], it is unclear whether there is a threshold Mg2+ ion release over which improved bone formation is achieved. This knowledge would help discriminate the effects of different Mg^{2+} ion release rates from Mg-based implants. Alternatively, the increase in NBF and BIC observed in the J1 group could be attributed to the release of Sr^{2+} ions. Recent studies showed that the local and controlled release of Sr^{2+} ions from titania nanotubes enhanced the BIC when implanted in the medullar cavity of rats for 2 weeks [8]. The authors proposed that the release of Sr^{2+} ions could be incorporated into the local milieu of a variety of implants to accelerate bone ingrowth and improve osseointegration.

In response to the beneficial effects of Sr^{2+} ion release, a variety of strategies have been proposed including the incorporation of Sr^{2+} into ceramic coatings, bioactive glasses, etc [6,55,56]. The advantage of incorporating Sr^{2+} ions into the bulk of Mg alloy, such as the J1 alloy, resides in the stable and continued ion release (Figs. 5, 9 and 12) to achieve the stimulatory effects leading to increased NBF. In addition, bulk alloys provide more mechanical stability and integrity compared with other strategies (i.e. coatings) that seek to incorporate Sr^{2+} ions. Our results showed significant increases in NBF, BIC and expressions of osteogenic genes which were likely induced by the stable release of Sr^{2+} ions from the degradation of the J1 alloy (Figs. 5, 9 and 12).

The release of Sr^{2+} ions during the degradation of the J1 implant did not induce detrimental long-term systemic effects. Previous studies indicated that intravenous administration of $SrCl_2$ (2000 mg kg^{-1} per day) [57] was not lethal to mice. The corrosion rate of the J1 alloy was approximately 0.73 mm y^{-1}, at this rate the total Sr^{2+} ion release of the applied implant device in this study was smaller than 0.022 mg kg^{-1} per day (calculated by the total surface area and the corrosion rate, 0.73 $\pm$ 0.05 mm y^{-1}) which is also significant lower than the clinical dose recommended for strontium ranelate (5–20 mg kg^{-1} per day) [58]. Although dose is the most important factor when talking about toxicology, significant lower exposed dose (0.022 mg kg^{-1} per day) compared with published studies applied in this work assured its safety as implant device [8,10].

Furthermore, although an increase in the Sr^{2+} ion content in the liver was observed at 2w post-implantation, near-homeostatic levels were nearly recovered at

16w. Similarly, although an increase in the Sr^{2+} ion concentration in the blood plasma was observed from 2w-8w post-implantation, the lack of statistically significant differences indicated that the rabbits were able to effectively metabolize the Sr^{2+} ions being released. Our results also suggest that a more detrimental effect on inflammation, cardiac, and hepatic functions was caused by the enhanced release of Mg^{2+} ions from the pure Mg control (i.e. faster corrosion rate compared with the J1 group, Fig. 7 and 8). Further studies are necessary to directly determine the in vivo release rate of Sr^{2+} as a result from the degradation of the J1 alloy implant to ensure that clinically therapeutic doses are not exceeded.

5 Conclusions

This study has shown that J1 alloy had a statistically significantly appropriate corrosion and biocompatible properties, while showed proof of enhanced effects of stimulation to new bone formation after implantation in test animals. The 16 weeks implantation of the J1 alloy in the test animals did not significantly alter 16 primary indexes of hematology, cardiac damage, inflammation, hepatic functions and metabolic process, and no abnormal physiology or diseases were observed after implantation. The peri-implant bone formation as well as the expressions of four osteogenesis related genes was significantly increased for J1 implant group 16 weeks post-implantation compared to the Mg reference group. Moreover, long lasting and stable Sr element release was found throughout the entire degradation period. The sound osteogenic properties and stimulation effect on bone formation suggest its very attractive clinical potential.

Acknowledgments

The authors thank for the supports of National Natural Science Foundation of China under Grant Nos. 51504065 and 51474063, the Fundamental Research Funds for the Central Universities, Northeastern University No. N130302007, and Hellman Faculty Fellowship (HL).

References

1. P.J. Meunier, C. Roux, E. Seeman, S. Ortolani, J.E. Badurski, T.D. Spector, J. Cannata, A. Balogh, E.M. Lemmel, S. Pors-Nielsen, R. Rizzoli, H.K. Genant, J.Y. Reginster, The effects of strontium ranelate on the risk of vertebral fracture in women with postmenopausal osteoporosis, New England J. Med. 350 (2004) 459–468.

2. E. Seeman, B. Vellas, C. Benhamou, J.P. Aquino, J. Semler, J.M. Kaufman, K. Hoszowski, A.R. Varela, C. Fiore, K. Brixen, J.Y. Reginster, S. Boonen, Strontium ranelate reduces the risk of vertebral and nonvertebral fractures in women eighty years of age and older, J. Bone Miner. Res.: Off. J. Am. Soc. Bone Miner. Res. 21 (2006) 1113–1120.

3. E. Bonnelye, A. Chabadel, F. Saltel, P. Jurdic, Dual effect of strontium ranelate: stimulation of osteoblast differentiation and inhibition of osteoclast formation and resorption in vitro, Bone 42 (2008) 129–138.

4. J. Braux, F. Velard, C. Guillaume, S. Bouthors, E. Jallot, J.M. Nedelec, D. LaurentMaquin, P. Laquerriere, A new insight into the dissociating effect of strontium on bone resorption and formation, Acta Biomater. 7 (2011) 2593–2603.

5. J. Coulombe, H. Faure, B. Robin, M. Ruat, In vitro effects of strontium ranelate on the extracellular calcium-sensing receptor, Biochem. Biophys. Res. Commun. 323 (2004) 1184–1190.

6. H. Zreiqat, Y. Ramaswamy, C. Wu, A. Paschalidis, Z. Lu, B. James, O. Birke, M. McDonald, D. Little, C.R. Dunstan, The incorporation of strontium and zinc into a calcium-silicon ceramic for bone tissue engineering, Biomaterials 31 (2010) 3175–3184.

7. C. Capuccini, P. Torricelli, F. Sima, E. Boanini, C. Ristoscu, B. Bracci, G. Socol, M. Fini, I.N. Mihailescu, A. Bigi, Strontium-substituted hydroxyapatite coatings synthesized by pulsed-laser deposition: in vitro osteoblast and osteoclast response, Acta Biomater. 4 (2008) 1885–1893.

8. L. Zhao, H. Wang, K. Huo, X. Zhang, W. Wang, Y. Zhang, Z. Wu, P.K. Chu, The osteogenic activity of strontium loaded titania nanotube arrays on titanium substrates, Biomaterials 34 (2013) 19–29.

9. U. Thormann, S. Ray, U. Sommer, T. ElKhassawna, T. Rehling, M. Hundgeburth, A. Henß, M. Rohnke, J. Janek, K.S. Lips, C. Heiss, G. Schlewitz, G. Szalay, M. Schumacher, M. Gelinsky, R. Schnettler, V. Alt, Bone formation induced by strontium modified calcium phosphate cement in critical-size metaphyseal fracture defects in ovariectomized rats, Biomaterials 34 (2013) 8589–8598.

10. W. Zhang, Y. Shen, H. Pan, K. Lin, X. Liu, B.W. Darvell, W.W. Lu, J. Chang, L. Deng, D. Wang, W. Huang, Effects of strontium in modified biomaterials, Acta Biomater. 7 (2011) 800–808.

11. O.Z. Andersen, V. Offermanns, M. Sillassen, K.P. Almtoft, I.H. Andersen, S. Sorensen, C.S. Jeppesen, D.C. Kraft, J. Bottiger, M. Rasse, F. Kloss, M. Foss, Accelerated bone ingrowth by local delivery of strontium from surface functionalized titanium implants, Biomaterials 34 (2013) 5883–5890.

12. M.P. Staiger, A.M. Pietak, J. Huadmai, G. Dias, Magnesium and its alloys as orthopedic biomaterials: a review, Biomaterials 27 (2006) 1728–1734.

13. K.U. Kainer, P. Bala Srinivasan, C. Blawert, W. Dietzel, 3.09 – Corrosion of Magnesium and its Alloys, in: B. Cottis, M. Graham, R. Lindsay, S. Lyon, T. Richardson, D. Scantlebury, H. Stott (Eds.), Shreir's Corrosion, Elsevier, Oxford, 2010. pp. 2011–2041.

14. F. Witte, The history of biodegradable magnesium implants: a review, Acta Biomater. 6 (2010) 1680–1692.

15. H.M. Wong, Y. Zhao, V. Tam, S. Wu, P.K. Chu, Y. Zheng, M.K.T. To, F.K.L. Leung, K.D.K. Luk, K.M.C. Cheung, K.W.K. Yeung, In vivo stimulation of bone formation by aluminum and oxygen plasma surface-modified magnesium implants, Biomaterials 34 (2013) 9863–9876.

16. S.A. Chacko, J. Sul, Y. Song, X. Li, J. LeBlanc, Y. You, A. Butch, S. Liu, Magnesium supplementation, metabolic and inflammatory markers, and global genomic and proteomic profiling: a randomized, double-blind, controlled, crossover trial in overweight individuals, Am. J. Clin. Nutr. 93 (2011) 463–473.

17. R.R. Breaker, G.F. Joyce, A DNA enzyme with Mg(2+)-dependent RNA phosphoesterase activity, Chem. Biol. 2 (1995) 655–660.

18. P. Flatman, Magnesium transport across cell membranes, J. Membrain Biol. 80 (1984) 1–14.

19. L. Wu, B.J. Luthringer, F. Feyerabend, A.F. Schilling, R. Willumeit, Effects of extracellular magnesium on the differentiation and function of human osteoclasts, Acta Biomater. 10 (2014) 2843–2854.

20. R. Schwartz, A.H. Reddi, Influence of magnesium depletion on matrix-induced endochondral bone formation, Calcified Tissue Int. 29 (1979) 15–20.

21. H.M. Wong, S. Wu, P.K. Chu, S.H. Cheng, K.D.K. Luk, K.M.C. Cheung, K.W.K. Yeung, Low-modulus Mg/PCL hybrid bone substitute for osteoporotic fracture fixation, Biomaterials 34 (2013) 7016–7032.

22. D. Tie, F. Feyerabend, W.D. Mueller, R. Schade, K. Liefeith, K.U. Kainer, R. Willumeit, Antibacterial biodegradable Mg–Ag alloys, Eur. Cells Mater. 25 (2013) 284–298. discussion 298.

23. S. Feliu Jr, A. Samaniego, V. Barranco, A.A. El-Hadad, I. Llorente, P. Adeva, The effect of low temperature heat treatment on surface chemistry and corrosion resistance of commercial magnesium alloys AZ31 and AZ61 in 0.6 M NaCl solution, Corros. Sci. 80 (2014) 461–472.

24. R.-G. Guan, A.F. Cipriano, Z.-Y. Zhao, J. Lock, D. Tie, T. Zhao, T. Cui, H. Liu, Development and evaluation of a magnesium–zinc–strontium alloy for biomedical applications – Alloy processing, microstructure, mechanical properties, and biodegradation, Mater. Sci. Eng. C 33 (2013) 3661–3669.

25. X.N. Gu, X.H. Xie, N. Li, Y.F. Zheng, L. Qin, In vitro and in vivo studies on a Mg–Sr binary alloy system developed as a new kind of biodegradable metal, Acta Biomater. 8 (2012) 2360–2374.

26. A.F. Cipriano, T. Zhao, I. Johnson, R.G. Guan, S. Garcia, H. Liu, In vitro degradation of four magnesium-zinc-strontium alloys and their cytocompatibility with human embryonic stem cells, J. Mater. Sci.: Mater. Med. 24 (2013) 989–1003.

27. ASTM. Standard Practice for Codification of Certain Nonferrous Metals and Alloys, Cast and Wrought. ASTM B275, 2013.

28. M. Nicolas, A. Deschamps, Characterisation and modelling of precipitate evolution in an Al–Zn–Mg alloy during non-isothermal heat treatments, Acta Mater. 51 (2003) 6077–6094.

29. CAN/CSA-ISO. Biological Evaluation of Medical Devices, Part 4: Selection of Tests for Interactions with Blood. CAN/CSA-ISO 10993.4-97. 2006, vol. CAN/ CSA-ISO 10993.4-97.

30. X. Gu, Y. Zheng, Y. Cheng, S. Zhong, T. Xi, In vitro corrosion and biocompatibility of binary magnesium alloys, Biomaterials 30 (2009) 484–498.

31. The State scientific and technological commission of China. Regulations for the Administration of Affaires Concerning Experimental Animals. Online, 2011. Available from URL: <http://www.gov.cn/gongbao/content/2011/content_1860757.htm>.

32. N. Erdmann, N. Angrisani, J. Reifenrath, A. Lucas, F. Thorey, D. Bormann, A. Meyer-Lindenberg, Biomechanical testing and degradation analysis of

MgCa0.8 alloy screws: a comparative in vivo study in rabbits, Acta Biomater. 7 (2011) 1421–1428.

33. K.A. Pasyk, C.A. Hassett, Modified hematoxylin and eosin staining method for epoxy-embedded tissue sections, Pathol. Res. Pract. 184 (1989) 635–638.

34. B.R. Don, G. Kaysen, Serum albumin: relationship to inflammation and nutrition, Semin. Dial. 17 (2004) 432–437.

35. J.T. Martins, D.J. Li, L.B. Baskin, I. Jialal, J.H. Keffer, Comparison of cardiac troponin I and lactate dehydrogenase isoenzymes for the late diagnosis of myocardial injury, Am. J. Clin. Pathol. 106 (1996) 705–708.

36. E. Giannini, F. Botta, A. Fasoli, P. Ceppa, D. Risso, P.B. Lantieri, G. Celle, R. Testa, Progressive liver functional impairment is associated with an increase in AST/ ALT ratio, Dig. Dis. Sci. 44 (1999) 1249–1253.

37. M.W. Pfaffl, G.W. Horgan, L. Dempfle, Relative expression software tool (REST (c)) for group-wise comparison and statistical analysis of relative expression results in real-time PCR, Nucleic Acids Res. 30 (2002).

38. P.S. Cerri, E. Sasso-Cerri, Staining methods applied to glycol methacrylate embedded tissue sections, Micron 34 (2003) 365–372.

39. F.E. Wang, F.A. Kanda, C.F. Miskell, A.J. King, Comments on the crystal structures of Ba_2Mg_{17}, and Sr_2Mg_{17}, Acta Crystallogr. A 16 (1963) 697–698.

40. A.A. Nayeb-Hashemi, J.B. Clark, The Mg–Sr (Magnesium-Strontium) system, Bull. Alloy Phase Diagrams 7 (1986) 149–156.

41. D. Tie, F. Feyerabend, N. Hort, R. Willumeit, D. Hoeche, XPS studies of magnesium surfaces after exposure to Dulbecco's modified eagle medium, Hank's buffered salt solution, and simulated body fluid, Adv. Eng. Mater. 12 (2010) B699–B704.

42. S. Ardizzone, C.L. Bianchi, M. Fadoni, B. Vercelli, Magnesium salts and oxide: an XPS overview, Appl. Surf. Sci. 119 (1997) 253–259.

43. P.J. Kelly, J.B. Bassingthwaighte, Studies on bone ion exchanges using multipletracer indicator-dilution techniques, Fed. Proc. 36 (1977) 2634–2639.

44. S.A. Argyropoulos, G.L.S. Chow, An experimental investigation on the assimilation and recovery of strontium–magnesium alloys in A356 melts, J. Light Met. 2 (2002) 253–262.

45. H.S. Brar, J. Wong, M.V. Manuel, Investigation of the mechanical and degradation properties of Mg–Sr and Mg–Zn–Sr alloys for use as potential biodegradable implant materials, J. Mech. Behav. Biomed. Mater. 7 (2012) 87–95.

46. K. Hazeli, A. Sadeghi, M.O. Pekguleryuz, A. Kontsos, Damping and dynamic recovery in magnesium alloys containing strontium, Mater. Sci. Eng. A 589 (2014) 275–279.

47. D. Tie, F. Feyerabend, N. Hort, D. Hoeche, K.U. Kainer, R. Willumeit, W.D. Mueller, In vitro mechanical and corrosion properties of biodegradable Mg–Ag alloys, Mater. Corros. 65 (2014) 569–576.

48. X. Zhang, Z. Ba, Q. Wang, Y. Wu, Z. Wang, Q. Wang, Uniform corrosion behavior of GZ51K alloy with long period stacking ordered structure for biomedical application, Corros. Sci. 88 (16) (2014) 1–5.

49. L. Choudhary, R.K. Singh Raman, J. Hofstetter, P.J. Uggowitzer, In-vitro characterization of stress corrosion cracking of aluminium-free magnesium alloys for temporary bio-implant applications, Mater. Sci. Eng. C 42 (2014) 629–636.

50. D. Persaud-Sharma, A. McGoron, Biodegradable magnesium alloys: a review of material development and applications, J. Biomimetics Biomater. Tissue Eng. 12 (2012) 25–39.

51. M. Bornapour, M. Celikin, M. Cerruti, M. Pekguleryuz, Magnesium implant alloy with low levels of strontium and calcium: the third element effect and phase selection improve bio-corrosion resistance and mechanical performance, Mater. Sci. Eng. C 35 (2014) 267–282.

52. Y. Zhao, M.I. Jamesh, W.K. Li, G. Wu, C. Wang, Y. Zheng, K.W.K. Yeung, P.K. Chu, Enhanced antimicrobial properties, cytocompatibility, and corrosion resistance of plasma-modified biodegradable magnesium alloys, Acta Biomater. 10 (2014) 544–556.

53. H. Liu, The effects of surface and biomolecules on magnesium degradation and mesenchymal stem cell adhesion, J. Biomed. Mater. Res.: Part A 99 (2011) 249– 260.

54. G. Williams, H.N. McMurray, R. Grace, Inhibition of magnesium localised corrosion in chloride containing electrolyte, Electrochim. Acta 55 (2010) 7824–7833.

55. Y. Li, Q. Li, S. Zhu, E. Luo, J. Li, G. Feng, Y. Liao, J. Hu, The effect of strontium substituted hydroxyapatite coating on implant fixation in ovariectomized rats, Biomaterials 31 (2010) 9006–9014.

56. M.T. Vestermark, E.-M. Hauge, K. Soballe, J.E. Bechtold, T. Jakobsen, J. Baas, Strontium doping of bone graft extender, Acta Orthopaedica 82 (2011) 614– 621.

57. R. Kroes, E.M. den Tonkelaar, A. Minderhoud, G.J. Speijers, D.M. Vonk-Visser, J. M. Berkvens, G.J. van Esch, Short-term toxicity of strontium chloride in rats, Toxicology 7 (1977) 11–21.

58. P.J. Meunier, D.O. Slosman, P.D. Delmas, J.L. Sebert, M.L. Brandi, C. Albanese, R. Lorenc, S. Pors-Nielsen, M.C. De Vernejoul, A. Roces, J.Y. Reginster, Strontium ranelate: dose-dependent effects in established postmenopausal vertebral osteoporosis–a 2-year randomized placebo controlled trial, J. Clin. Endocrinol. Metab. 87 (2002) 2060–2066.